Exp Astron (2006) 21:169–187
DOI 10.1007/s10686-007-9080-7

ORIGINAL ARTICLE

Design of a high update-rate star sensor for arcsec-level attitude determination from balloon-borne X/γ astronomy platforms

G. Palladino · A. Basili · G. Di Cocco · T. Franceschini · G. Landini · S. Silvestri · A. Barbini · M. Galimberti · L. A. Gizzi

Received: 27 October 2006 / Accepted: 5 September 2007 /
Published online: 17 October 2007

Abstract This paper describes the design of a star sensor based upon a high dynamic range CCD in order to reach an arcsec-level attitude determination in balloon-borne missions. A custom star identification software was developed and laboratory-tested on a prototype assembled using commercial components. A set of numerical simulations have been carried out to study the dependence on the pointing precision of the centroid position accuracy, the number of detected stars and the effect of the image focusing. Moreover, the role of the electronic noise and the discrete pixel structure on the light signals is identified by the analysis of numerical simulations. Laboratory tests confirm that the arcsec pointing accuracy with a 1 Hz update rate can be achieved with our combination of custom-developed software and selected hardware components.

Keywords Star sensor · CCD · Balloon-borne · Attitude control · Pointing precision · X-ray telescopes

1 Introduction – the HiPeG system

A new generation of high angular resolution X/γ-ray telescopes is presently being developed. Novel focusing techniques promise to extend the arcsec precision level

G. Palladino (✉) · A. Basili · G. Di Cocco · T. Franceschini · G. Landini · S. Silvestri
IASF, Istituto di Astrofisica Spaziale e Fisica cosmica,
INAF – Sezione di Bologna, 40129 Bologna, Italy
e-mail: palladino@iasfbo.inaf.it

G. Palladino
Dep. of Physics, University of Ferrara, Italy

A. Barbini · M. Galimberti · L. A. Gizzi
IPCF, Istituto per i Processi Chimico-Fisici, CNR – Area di Pisa, 56124 Pisa, Italy

obtained so far in the soft X-ray range to the 30–500 keV photon energy range. This is a major advance compared with collimated telescopes working in the same energy range, hardly capable of sub-deg resolution. In view of their approval as satellite missions (see for ex. [4]), these schemes require a proof of principle and test flights on board of balloon-borne platforms are typically used for these purposes. However, due to the severe requirements on pointing accuracy, new techniques are being developed to enhance the control and pointing performances of these platforms. Table 1 shows the anticipated performances of some of the european experiments that call for the best pointing accuracy ever needed on a balloon-borne flight.

These new X-ray optics, based on multilayer grazing incidence as well as on Bragg or Laue crystal diffraction, are characterized by large focal length and a relatively high angular resolution, typically much better than 1 arcmin. These features are a major concern in view of the implementation of the telescopes on balloon-borne platforms. In fact, the long focal length will require high aspect ratio telescope structures with consequent large (change of) moment of inertia (during zenith motion). Moreover, the high angular resolution and the very narrow field-of-view will require high pointing accuracy and stability of the platform during long exposure time.

Some telescopes of the new generation have already flown with attitude control systems specifically designed for high resolution guiding [7, 9]. In a recent work [3] it was demonstrated that arc-sec level pointing precision can indeed be achieved even in daytime conditions, using dedicated star camera systems. These studies suggest that several issues, including pointing error modelling and flexibility/efficiency of the star identification software/hardware need to be investigated in order to identify limiting factors in the pointing performance in a range of different experiments and operation conditions, from the normal tracking mode to the full solution of the "lost in space" condition.

In this context the HiPeG project (high performance gondola, an IASF-IPCF collaboration project, funded by the Italian Space Agency) aims at the development of a new, high performance software/hardware system for the attitude control of a balloon gondola carrying an X-ray telescope. A detailed account of the entire HiPeG system can be found elsewhere [1]. In this introduction we only give a short description of the HiPeG on-board system, in which the star sensor sub-system is logically integrated.

The HiPeG attitude measurement system consists of two absolute reference sensors: a group of four global positioning (GPS) receivers for a 3-D attitude information down to the arcmin level (about 1.8 arcmin) with a refresh frequency of 2 Hz and a star sensor, able to reach autonomously a pointing knowledge with

Table 1 Pointing performances required for some of the new generation of hard X-ray focusing telescopes

Telescope features	Grazing incidence (HEXIT)	Bragg diffraction (HAXTEL)	Laue diffraction (CLAIRE I-II)
Energy range (KeV)	20–70	60–150	170 (511)
Focal length (m)	~ 6	~ 5	2.76 (8.29)
Field of view (arcmin)	15	80	1 (15 arcsec)
Angular resolution (arcsec)	30	60	60 (15)

These instruments call for the best pointing accuracy ever needed on a balloon-borne flight.

a precision of 10 arcsec or better with a refresh rate of 1 Hz. This latter device is designed to be able to reconstruct the 3-D attitude of the gondola starting from a "lost in space" conditions, i.e. without any other information previously available on pointing direction. Anyway, the use of both devices is a good way to speed-up attitude calculation and guarantee an high precision level using a high frequency sampling of the measurement. Furthermore, the star sensor can work also in a "star tracker" mode, with some remarkable software simplification which does not alter its efficiency. At the occurrence of any calculation failure during the tracking mode, the device switches again to the "lost in space" working mode. In its final version the star sensor will be required to update the pointing attitude at a 1 Hz rate during night flight conditions. In the case of operation in daylight conditions, the sensor will be equipped with a telescopic baffle and a blue rejecting filter [10] to cut most of the sunlight (Rayleigh) scattered from the residual gas still present in the atmosphere at the balloon floating altitude (3–4 g/cm^2). To this purpose, an upgraded version of the entire system for a full-autonomous attitude system reliable for any flight condition will be completed after the analysis of data collected during a first night flight.

The combination of GPS and star sensor sub-systems have already been successfully employed in previous experiments and can be considered now a standard approach for high-accuracy attitude control systems [2, 6]. Nevertheless in the HiPeG system these devices need to be optimized to ensure flexibility for different flight conditions (e.g. experiment location, flight duration, variable star density for different field-of-view), and therefore fully adaptive as multi-purpose facilities for high-energy astronomy experiments.

Table 2 summarizes the HiPeG pointing performances. The pointing accuracy and the pointing stability are given for either a static pointing or dynamical tracking of a source. The pointing knowledge is equivalent to the minimum pointing precision level required from the star sensor.

In the present design the mechanical attitude control of the gondola will be accomplished by a motorized pivot mounted on the balloon cord in combination with a reaction wheel placed on the platform. In the order to reach and maintain the required pointing attitude, an on-board computer will process the GPS and the star sensor signals and will generates a "pointing correction" signal to drive and balance the gondola rotation. A series of tests and simulation were carried out to set the right software/hardware parameters to avoid any resonant oscillation of the system and disturbances during the star sensor acquisition time.

The main logic unit on-board consists of a CPU PC 104 to operate pointing correction with both GPS/star sensor data and a DSP to control the power consumption of electrical engines.

In this paper we focus only on a description of the star sensor sub-system. After a description of the hardware parameters, we illustrate the basic principles of the

Table 2 Pointing performance of the HiPeG attitude control system

Gondola requirements	Pointing accuracy	Pointing stability	Pointing knowledge
Goal	20 arcsec	60 arcsec	10 arcsec

The first and the second parameters are the maximum tolerance for gondola oscillation during static pointing or dynamic tracking of a source. The pointing knowledge is equivalent to the star sensor required minimum precision. All the parameters are 1-σ values.

Fig. 1 The star sensor prototype. Clearly visible *on the left*, mounted on the mechanical frame, are the CCD detector (*top*) and the dedicated computer hardware. *On the right* is the stainless steel vessel with optical window. In operating conditions an atmosphere of nitrogen will guarantee an efficient thermal exchange

custom-developed identification and tracking software and we show the results of laboratory tests performed on a prototype hardware system assembled using commercial components (see Fig. 1). Finally we present the result of a Monte Carlo simulation code developed to investigate the performance of the system and to evaluate the role of the main system parameters in the pointing reconstruction accuracy.

2 The star sensor prototype – the hardware

The HiPeG star sensor uses a compact SenSys digital camera (Roper Scientific), equipped with a Kodak KAF 400 CCD chip and an adjustable shutter. This camera features a thermoelectrically (Peltier) cooled array of 768×512 squared pixels of 9×9 μm size. The pixel signal is read by a data digitizer in the camera head (12 bits ADC). The camera ADC works in a "high dynamic range" mode, equivalent to a full-depth of 80,000 electrons (20 electrons per ADC level). The CCD readout speed of 1 MHz implies about 0.5 s for the full frame reading. Given the project requirement of 1 Hz for the refresh time of attitude measurement, this frame read-out time leaves a maximum of 0.5 s for both exposure time and star field identification/attitude calculation. As discussed below (see Section 7), in our case, the calculation time is expected to be around 15 ms, leaving a maximum exposure time of 485 ms. The CCD camera is equipped with an optics consisting of a nominal 105 mm photographic lens (Tamron) and with f/2.5 numerical aperture. This combination of optics and detector gives a rectangular field-of-view of about $4° \times 3°$ with a diffraction-limited spot size (calculated at a wavelength of 565 nm) of 3.4 μm FWHM, which is smaller than the CCD pixel size. The star sensor hardware is completed by a dedicated CPU, equipped with a Celeron Pentium III-900 MHz with 512 MB RAM and an AIA interface for the digital camera. The whole hardware is enclosed in a stainless vessel thermally coupled to the aluminium gondola structure. The vessel is pressurized at 1 atmosphere of nitrogen to provide thermal exchange and to prevent condensation.

The Peltier cooling keeps the CCD chip at a working temperature of 10°C with a stabilization of ±0.1°C, corresponding to a dark current of about 1.4 electrons per second per pixel, i.e. Moreover, a set of three temperature sensors (Dallas DS18S20 with range −55/+125°C and with resolution of ±0.5°C) are placed inside the vessel to monitor the temperature during operation. Some tests were carried out to evaluate the overall performance of the optics, especially in terms of sensitivity, optical aberration (e.g. field distortion) etc. Figure 4 shows the image of a camera field-of-view in the proximity of Vega, taken at sea level for a night exposure time of 10 s. The measured sensitivity of the camera is such that a eighth magnitude star, focused within one pixel, provides a signal of 1,000 ADC levels, which gives a signal of approximately 50 ADC levels for the maximum exposure time given above, corresponding to approximately 1,000 electrons.

3 The star sensor prototype – the software

Figure 2 shows the block diagram of the star identification software. A signal carrying the external parameters available to start the star pattern identification (i.e. coarse attitude coming from the GPS) and the protocol number of the requested mode of operation (e.g. the star identification only, target tracking, lens focusing mode, etc.) reaches the star sensor computer through a serial link and activates the routine named *Identification*. This routine performs the analysis of the image captured by the CCD to optimize the focusing condition. In fact, as it will be shown later (paragraph 4), the focusing of the image is one of the most critical issue for a high precision attitude determination. The routine named *Parameters* provides all the data generated by the program to the main on-board computer through a serial link. The routine named *Init*, executed only once during the program initialization, accomplishes the compilation of the star catalogue that includes all the parameters necessary to identify stars within a fixed magnitude range (Hipparcos digital catalogue from ESA, available at the URL http://astro.estec.esa.nl/SA-general/Projects/Hipparcos/hipparcos.html).

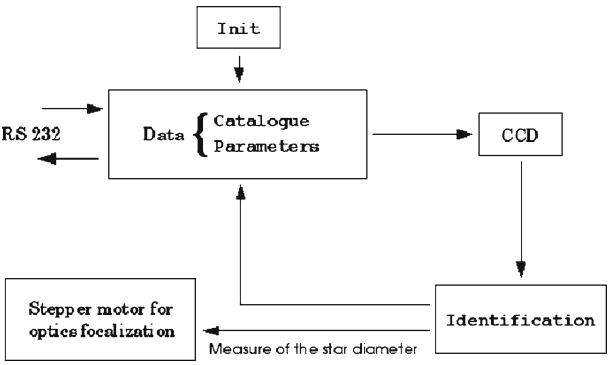

Fig. 2 The working scheme of the star sensor software. The serial link connects the star sensor own computer with the main HiPeG's CPU

3.1 The star location routine

The star sensor main software program consists of three separate and sequential algorithms (see also [5, 8]):

1. Algorithm 1 – location of the stars on the acquired CCD digital image;
2. Algorithm 2 – star identification and determination of the pointing direction;
3. algorithm 3 – tracking of the pointing direction to guide platform and telescope attitude stabilization.

The first algorithm locates the stars in the CCD image, rejecting fake star signals caused by electronic noise, lens internal reflections or diffuse atmospheric scattered optical background. An outline of the first algorithm is shown in Fig. 3.

In the algorithm, the threshold value is set to a fraction of the ADC level corresponding to the maximum of the pixel signal intensity histogram to avoid the effect of the diffuse optical background. After its calculation, executed at the start of any cycle of camera acquisition, this value is subtracted from the CCD signal. When the algorithm during the image scanning finds an illuminated pixel above threshold, the smallest rectangular area holding every other contiguous pixel above threshold becomes the frame in which the "center of gravity" of the signal intensity, i.e. the centroid of the selected pixels, is calculated. If the centroid position and the brighter pixel are found to be within a distance of two pixel, the centroid coordinates are stored in the computer memory; otherwise the rectangle starts to act as a new separate image to be scanned with higher thresholds. The program also stores the value of the mean star image diameter: this parameter will support the action of a specific algorithm able to reach the optimum focusing condition.

We point out here that the background level evaluation works better with an uniform sky foreground. In the case on non-uniform illumination (e.g. stray-light

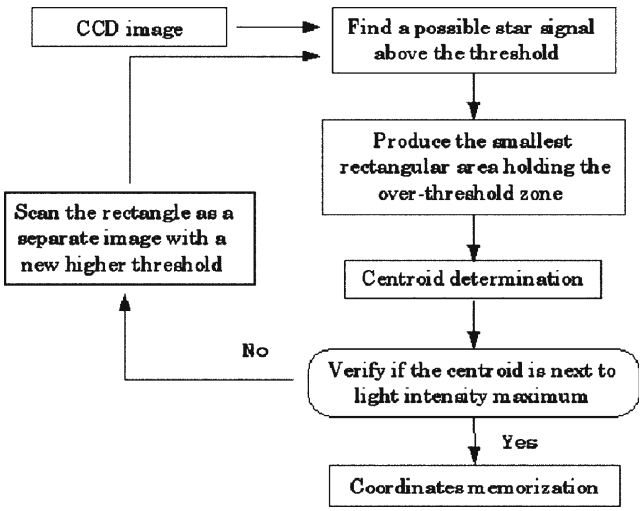

Fig. 3 Flow chart of the star location algorithm

illumination during daylight operation), the mean value of the signal coming from these pixels is subtracted from the total signal of the selected internal region.

3.2 The star identification algorithm

The second algorithm consists of four steps:

1. Identification of all possible centroids by comparing angular distances between any centroid and their neighbours with the angular distances between the catalogued stars in a sky area equivalent to the camera field-of-view;
2. Further selection by comparing, for every centroid, relative distances of neighbouring centroids and their geometrical arrangement with the corresponding catalogued stars. At the end of this step any identified centroid has one or more configurations of identified neighbouring centroids;
3. Execution of tree-path recursive cycles to make agreement within the identified centroid configurations and set the most probable of them;
4. Computation of the full 3-D camera attitude starting from the absolute (catalogued) position of identified centroids.

The first step of the algorithm computes the angular distances of every centroid with respect to all its neighbours present in the CCD field-of-view. Subsequently these distances are compared to the angular distances between all stars found in the Hipparcos catalogue and their neighbouring star groups, the most likely, if right, to be present in the camera field-of-view. If there are at least two distance agreements, the centroids of the initial configuration are marked as possible identified stars. If the GPS data are previously available, this step is done using a star catalogue reduced with an operation of "clipping" rather than using the full Hipparcos, i.e. the catalogue is reduced to a sky area slightly larger than the camera FOV around the actual pointing direction as measured from GPS receivers. The further verification, for every centroid, of the relative angular distances of their neighbours during the algorithm second step, allows the configurations of identified centroids which do not overlap correctly to be excluded, and assigns to every configuration a confidence level equivalent to the number of their own identified centroids. Starting from such a survivor configuration, the third step of the algorithm tries all possible combinations

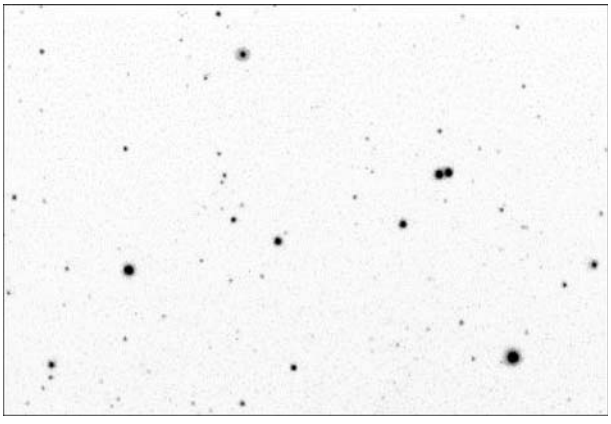

Fig. 4 A night-exposure image of the sky area in the proximity of Vega. The exposure time of the CCD camera is 10 s

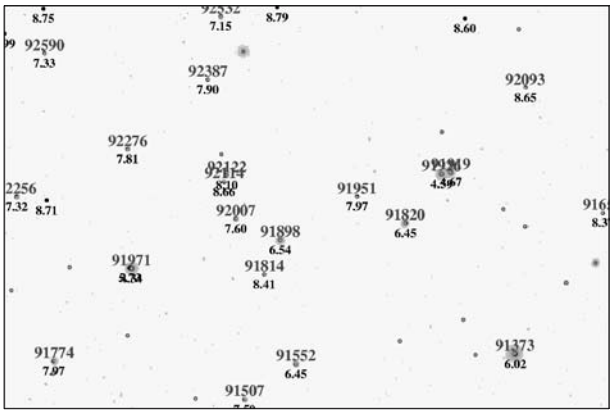

Fig. 5 The algorithm outline of the previous image. The identified stars are *labelled with their own Hipparcos number and magnitude*; the unidentified or fake stars are *marked as unnamed dots*. *Other little dots* are pixel groups found by the location algorithm above the threshold

of star "names" (Hipparcos identification code) which, during a path selection cycle, can arrange the configuration with the highest confidence level. Starting from the first possible "name" of the first centroid, every other possible star identification is weighted for compatibility by appropriate parameters (position, star "name", etc.). The "tree" is formed by trying, for every centroid, every different configuration of "names" which well "overlap" the neighbouring centroids. This cycle is recursive: starting from the first star field identification available, it tries to find the best match between any other alternative of star field identification which can maximize the number of identified stars. When the final centroid identification is done, the last step of the algorithm can determine the absolute camera attitude, and therefore the absolute pointing direction of the CCD normal axis.

A preliminary test of the star identification algorithms were carried out using images like the one shown in Fig. 4. The plot of Fig. 5 shows the same region of the sky of Fig. 4 after the algorithm analysis: every identified centroid is marked by the corresponding Hipparcos code number and magnitude (up to ninth). The image points with a magnitude index only are unidentified centroids, while the empty dots are fake stars due to spurious signals (noise over the threshold or internal reflections into the optics). According to these tests, no measurable distortion of the optical field was found.

3.3 The tracking algorithm

The last algorithm tracks the pointing attitude of the telescope. This algorithm will enable to lock the pointing of the telescope on the astronomical target during long exposure times. The algorithm outline is shown in Fig. 6.

When the star identification for an image is done, every identified star becomes a member of a new and smaller catalogue which can be used instead of the complete Hipparcos to reduce calculation time during the process of the following image. Since the pointing precision increases with the number of identified stars (see paragraph 6), if the new star identification is successful the algorithm tries to identify other compatible stars from the Hipparcos catalogue. If the tracking fails, the algorithm starts again in the previous identification mode.

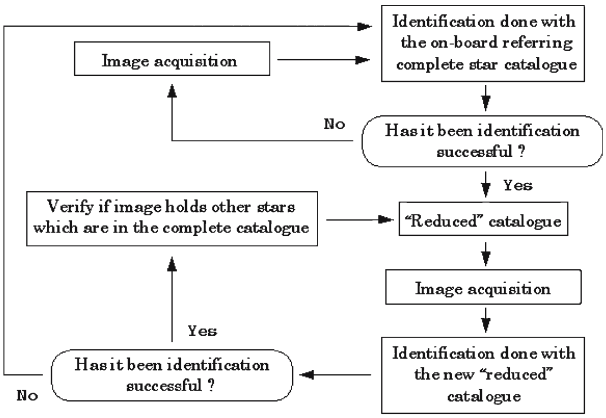

Fig. 6 Flow chart of the star tracking algorithm

4 Precision evaluation of the centroid coordinates

The design and construction of the star sensor prototype also required the investigation of those factors that can influence the final pointing precision. This was done first with an analytical model to study and optimize the various system parameters and then with a set of Monte Carlo simulations to test the algorithm reliability in operation-like conditions. The analytical model, in particular, has been developed to identify the main sources of uncertainty affecting the centroid determination and their propagation through the calculation.

The physical quantities included in the model that affect the centroid determination are the following:

1. The noise coming from each CCD pixel;
2. The quantization of the signal output of the ADC;
3. The discretization caused by the pixel geometry.

Considering the high dynamic range of the CCD used in our prototype (12 bit), the signal output quantization effect can be shown to be negligible. In contrast, the discretization effect is fundamental in centroid localization: by defining $\overline{E_{ij}}$ as the quantized ADC output (photoelectrons + the remaining noise fluctuations after background subtraction) for every pixel with center coordinates (x_i, y_i), the centroid coordinates (x_c, y_c) are:

$$x_c = \frac{\sum_{i=0}^{n_i-1} \sum_{j=0}^{n_j-1} x_i \overline{E_{ij}}}{\sum_{i=0}^{n_i-1} \sum_{j=0}^{n_j-1} \overline{E_{ij}}} \tag{1}$$

$$y_c = \frac{\sum_{i=0}^{n_i-1} \sum_{j=0}^{n_j-1} y_i \overline{E_{ij}}}{\sum_{i=0}^{n_i-1} \sum_{j=0}^{n_j-1} \overline{E_{ij}}} \tag{2}$$

where i and j are respectively the index numbers of the pixels along the long and the short side of the $n_i \times n_j$ rectangle selected by the star location algorithm.

Considering only the abscissa coordinate, (1) can be written as:

$$x_c = \frac{\sum_{ij} x_i \overline{E_{N_{ij}}} + x_0 \overline{E_0}}{\sum_{ij} \overline{E_{N_{ij}}} + \overline{E_0}} \tag{3}$$

where $\overline{E_{N_{ij}}}$ is the pixel noise, x_0:

$$x_0 = \frac{\sum_{ij} x_i \overline{E_{0_{ij}}}}{\sum_{ij} \overline{E_{0_{ij}}}} \tag{4}$$

is the centroid abscissa calculated in the absence of noise and $\overline{E_0}$ the sum of the noiseless signals $\overline{E_{0_{ij}}}$ integrated over all pixels. Centroid coordinate x_c (3) is actually a function Φ of the pixel noise $\overline{E_{N_{ij}}}$ and of the coordinate x_0, and therefore the quadratic error affecting the centroid abscissa is:

$${\sigma_{x_c}}^2 = \sum_{ij} \left(\frac{\partial \Phi}{\partial \overline{E_{N_{ij}}}} \right)^2 {\sigma_{N_{ij}}}^2 + \left(\frac{\partial \Phi}{\partial x_0} \right)^2 {\sigma_{x_0}}^2 \tag{5}$$

where $\sigma_{N_{ij}}$ and σ_{x_0} are respectively the pixel noise fluctuations and the abscissa uncertainty due to pixel discretization of the noiseless component of the signal.

If the mean value of the abscissa x_0 is supposed to be equal to the central position along the sides of the $n_i \times n_j$ pixel rectangle, by calculating the first term of the sum (5) assuming for simplicity $n_i = n_j = n$ and the noise fluctuation σ_N constant for every pixel, we finally find:

$$\sigma_{noise} = \frac{n}{\overline{E_0}} \frac{\sqrt{n^2 - 1}}{2\sqrt{3}} \sigma_N \, . \tag{6}$$

The noise component of the centroid error is therefore inversely proportional to the signal intensity of the single pixel and directly proportional to the noise amplitude. The plot of Fig. 7 shows the behaviour of the noise component for different values of star image diameters (expressed in pixels) and SNR ratio: this quantity, independent of the star size, is the ratio between the total signal intensity of one star (integrated over pixels and measured in ADC levels) and the noise fluctuation coming from one pixel and measured to be five ADC levels. The behaviour close to n^2 for large star images ($n > 10$) shows a significant influence of this noise when the number of pixels involved in the centroid determination becomes very large. At the same time the error on the centroid abscissa increases when the star signal decreases.

A further simplification has been included in the model to obtain an analytical estimate of the "discretization" term σ_{x_0} in (5). The pixel discretization effect depends on the "shape overlapping" of the star image into the CCD plane: by changing the position of the star center, the pixel signal along the image envelope can modify the value of the centroid position. If the shape of the star intensity is assumed to be constant, it becomes possible to build a simple analytical model to interpret the qualitative behaviour of this discretization term. The results of this simple model

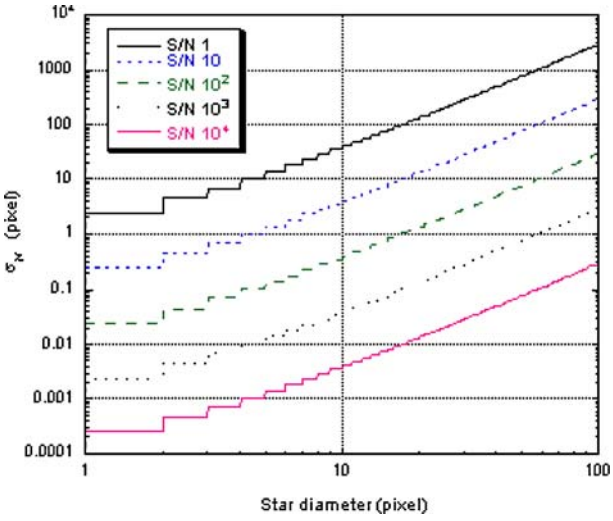

Fig. 7 The noise component on centroid location error depends on star image size and star intensity. The signal to noise ratio is the ratio between the total signal of a star and the noise fluctuation coming from one pixel (equivalent to five ADC levels)

will be compared with a more realistic case in paragraph 7. This qualitative model assumes a squared signal distribution $P(x)$:

$$P(x) = \begin{cases} a & x_r \le x \le (x_r + L) \\ 0 & x < x_r, x > (x_r + L) \end{cases} \tag{7}$$

where x_r is the variable edge position of a parallelepiped of side L and height a. The total signal intensity is:

$$\overline{E_0} = \sum_{ij} \overline{E_{0_{ij}}} = aL^2 \,. \tag{8}$$

The abscissa of the centroid position is now (see (4)):

$$x_0 = \frac{1}{aL} \sum_{i=0}^{n_x - 1} \left(i + \frac{1}{2}\right) l \overline{E_{0_{ij}}} \tag{9}$$

where l is the length of the pixel size.

The effect of the discretization resides in the value of the signal integrated on the pixel with coordinates i, j along the shape edge:

$$\overline{E_{0_{ij}}} = \int_{il}^{(i+1)l} P(x)\, \mathrm{d}x \,. \tag{10}$$

Considering the shape described by (7), the value of (10) depends on the different intervals of integration. By calculating the values of the integral (10) as RMS value by varying L (for length values equal or bigger than 1 pixel) and the position x_0 in 1,000 different positions on the camera chip, we obtain for the discretization error the behaviour showed in Fig. 8: the "bounces" visible in the plot occur when the value of $[L]$ is an integer number of pixels, while the zero points correspond to $[L] = L$. The overall behaviour is inversely proportional to the "star" size: a large

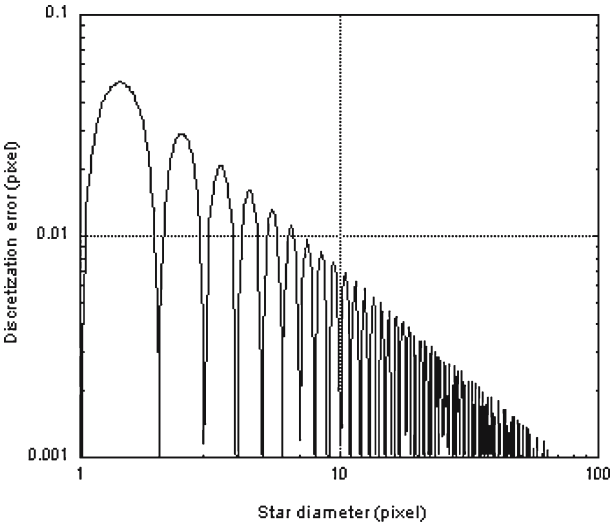

Fig. 8 The discretization component on centroid location error gets smaller for large star images and is independent from the star intensity. The results of the analysis showed here is valid only if the diameter of the star image is bigger than one pixel

star image suffers less discretization effects because of the minor importance of the signal coming from the pixels along the edge of the shape during centroid calculation. Finally, we observe that the discretization effect is independent of the signal intensity.

Figure 9 shows the behaviour of the total centroid error estimation function of the star image diameter (measured in pixels) for the SNR value of 10^3 ADC levels (i.e. a star signal of 5,000 ADC levels "spread" over L^2 pixels). The error sum gives a curve with a minimum: the discretization effect is dominant for small sized star images, while the noise effect starts to dominate when the star image size becomes larger. This feature therefore suggests that, once the SNR value is fixed, a value of the diameter of the star image exists (i.e. a focusing position of the optics) that minimizes

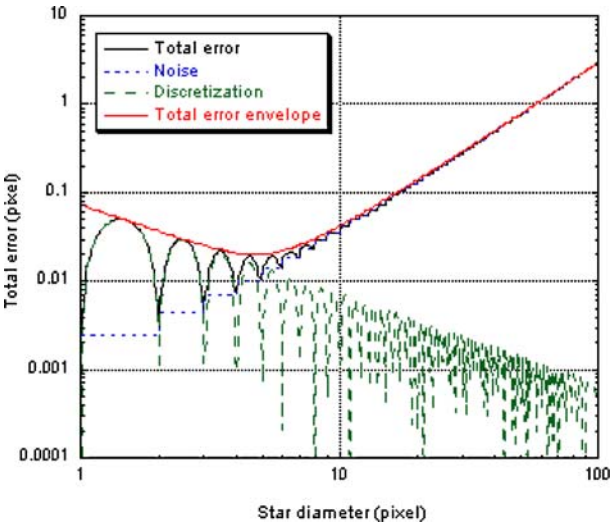

Fig. 9 The total error on centroid location for a SNR value of 10^3. The envelope curve has a visible minimum point

the error affecting the centroid coordinates. This behaviour, compared with the plot at Fig. 7, suggests that the cross-over point between noise and discretization effects will depend also on the total signal.

5 Test on the centroid precision

To verify the centroid precision model, a Monte Carlo test has been executed on the star location algorithm. Every star has been simulated like a bi-dimensional gaussian point spread function with total intensity and width. The center of the distribution has been randomly placed on the whole CCD surface to test different effects of pixel discretization.

The dynamic range of the simulated CCD was set to be 12 bit and the noise fluctuation was set at $\sigma_N = 5$ ADC levels. The simulation tested 10^3 stars for every SNR intensity ranging from 10 to 10^5 (independent from the star diameter) and for every value of star diameter (i.e. the FWHM of the gaussian flux distribution) varying from 0.2 to 20 (measured in pixels). The code of simulation provides also the effect of pixel saturation.

The plot of Fig. 10 shows the RMS value of the centroid position over 1,000 trials. These results confirm the qualitative behaviour of the centroid error suggested by the model in Fig. 9: an optimum value exists that minimizes the centroid error. Below that value the effect of the pixel discretization dominates while for values above the centroid error is caused by noise fluctuations. The plot of Fig. 10 also shows the behaviour of the data for higher SNR values of 10^4 and 10^5, similar to the characteristic "bounces" of the discretization effect seen in the analytical model of the "square star". This behaviour can be explained by considering the total measured intensities: in the case of simulated pixel saturation, the star shape becomes similar to an uniform and almost squared distribution because of a cut-off effect on the gaussian point spread function.

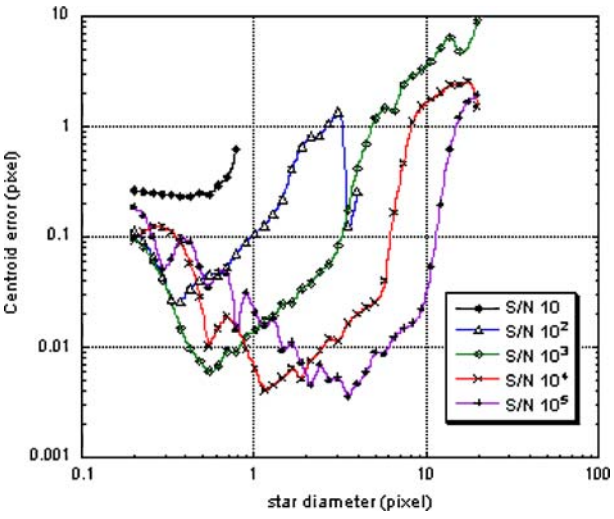

Fig. 10 Output of the Monte Carlo test on the total error affecting the centroid location. The centroid error, expressed as RMS error over 1,000 simulation trials, is a function of acquired star diameters for different SNR values. Error unit is given in number of CCD pixels

These circumstances, as described by the plot of Fig. 10, suggest that it is plausible to assume that the minimum error on the centroid location is as small as 1/10 of the pixel size over a wide range of values of star magnitude (10^2–10^4 SNR values), provided the star "width" is equivalent to the size of a single pixel. Such a result can be obtained by applying an appropriate star focusing procedure using the values of σ_x and σ_y as measured by the star sensor software as a guiding parameters. Since the occurrence of the blooming effect can degrade the centroid precision, we must prevent pixel saturation and keep the maximum number of electrons per pixel well below the full well capacity limit of 80,000 (4,000 ADC levels). In other words, this condition sets an upper limit to the star magnitude. Rescaling the measured data (see paragraph 2) to the maximum allowed exposure time of 0.5 s and assuming a light absorption in the atmosphere in the visible range equivalent to the 50%, we can infer a bright limit sensitivity up to stars of the 3^{rd} magnitude. The lower limit is given by the CCD sensitivity, that, assuming a total noise level of 5 ADC levels, ensures a S/N ratio of 3 with a ninth magnitude star.

6 Test on the pointing precision

A Monte Carlo test has been carried out to understand how the centroid errors propagate and influence pointing precision. The simulation used a range of number of centroids (from 3 to 100) with known coordinates shifted along an arbitrary direction around the initial point by a quantity equivalent to one pixel size. This choice, because of the linearity of the calculations involved in the attitude determination, allows error values as a reference to be obtained: the behaviour of the attitude precision in the presence of a wider or a narrower centroid error can be therefore derived from these error values times the appropriate offset factor.

The plot of Fig. 11 shows the pointing precision expressed as the variance of the vectorial differences between the calculated and nominal pointing direction (i.e. not

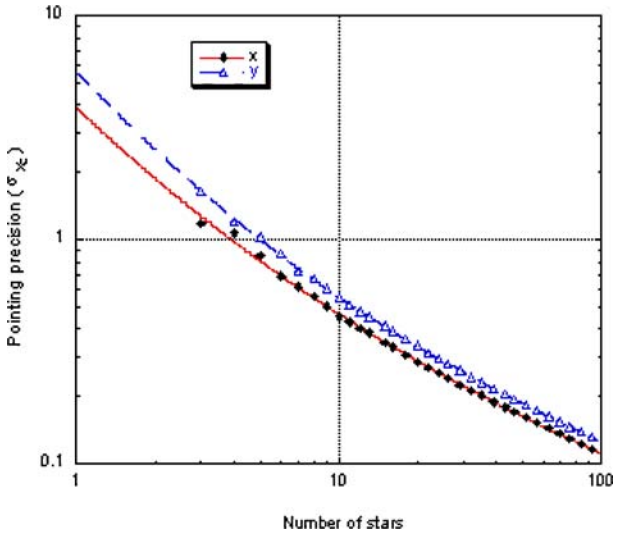

Fig. 11 Output of the Monte Carlo test on pointing precision as a function of the number of identified stars. Error unit is given as function of centroid precision (see text)

affected by the introduced centroid error); the vector components of the differences are along the CCD x (long) side and y (short) side. A total of 10^5 events were taken into account in the simulation for every number of centroids. In the same figure the pointing error is expressed in centroid error unit σ_{x_c}. The slightly different precision along x and y axes can be attributed to the calculation of the boresight direction during the pointing determination of the camera: that calculation, indeed, matters with centroid separation in a rectangular field.

The same figure shows that over a number of about ten stars the pointing error decreases inversely to the square root of the number of identified stars. Because the star identification algorithm uses the focal length as a parameter to calculate and compare the distances between stars, this result gives some conclusions about the role of the focal length value. Assuming an uniform density of stars in the sky, the number of stars acquired by the CCD camera will be proportional to the area of the field of view and therefore inversely proportional to the square of the focal length:

$$N_{\text{star}} \propto \frac{1}{(\text{focal length})^2} \,. \tag{11}$$

On the other hand the angular amplitude α of the single pixel is also a function of the focal length as:

$$\alpha \propto \frac{1}{\text{focal length}} \,. \tag{12}$$

These considerations can be used to show that the pointing precision is independent of the focal length. In fact, the pointing precision can be expressed as a function of its angular amplitude as the quantity σ_x (or σ_y, measured in number of pixels) times the pixel angular amplitude α. Considering (11) and (12), the pointing precision can be written as:

$$\sigma_{attitude} \approx \sigma_x (or\ \sigma_y)\sigma_{x_c}\alpha \approx \frac{\alpha}{\sqrt{N_{\text{star}}}} \propto 1 \,. \tag{13}$$

At this point the choice of the focal length of about 100 mm can be suggested by some considerations on the lower and upper limit on this parameter with the required performance of the system. The lower limit on the focal length is set by the small pixel size necessary to achieve the required measurement precision and by the necessity to limit the foreground light which increases as the square of the pixel size. The upper limit on the focal length, otherwise, is set mainly by the need to have a catalogue of manageable number of stars and a reasonable detector size. The output of the star identification simulations illustrated in the next paragraph suggests that the previous statistical considerations are still valid in the presence of a reasonable number of acquired stars.

7 Test on simulated images

Our set of numerical studies on the star sensor performances include a full simulation aimed at evaluating the behaviour of the whole star identification program during pointing and tracking operations.

Table 3 Test data on the star identification software using simulated images: case with 100 mm focal length

Focal length (mm)	Num. of stars	Ident. rate	Calc. time (s)
100	47–51	95.9%	$\bar{t} = 0.15 \pm 0.01$

In order to simulate a realistic star identification, a synthetic sky area around Cygnus X-1 was built with star coordinates and magnitude values up to ninth level from Hipparcos catalogue. The camera field of view was set to be $4° \times 3°$ wide, corresponding to the 100 mm focal length for our optics. The star point spread functions was extrapolated from the data obtained during the star identification test on real images and re-calibrated using an atmospheric absorption of 50% and a reference exposure time of 1 s. The simulation foresees the tracking of Cygnus X-1 "locked" at its astronomical coordinates (ascension 19 h 58 m 21.68 s, declination $35°12'5.8''$) from the 23.00 U.T. up to 00.00 U.T. of the 1th of July 2004 at 40 km of altitude above the ASI balloon facility of Milo (longitude $-12.35°$, latitude $38.01°$). A noise equivalent to five ADC levels has also been introduced on the images. A total of 3,600 consecutive images were used to simulate tracking operations. The simulation code was executed on a computer equipped with a Pentium IV – 1.8 GHz processor and a 512 MB RAM.

The test output confirms that star identification and tracking algorithms perform correctly during the slow apparent rotation of the field of view around Cygnus X-1. The columns of Table 3 show the data from the analysis of the 3,600 test images (i.e. one per second): the minimum and maximum number of stars, the percentage of identified stars and the calculation time needed to achieve the pointing direction.

The plots of Fig. 12(left) and (right) show respectively the spatial and the radial distribution of the calculated pointing direction around the target. The curve fit on

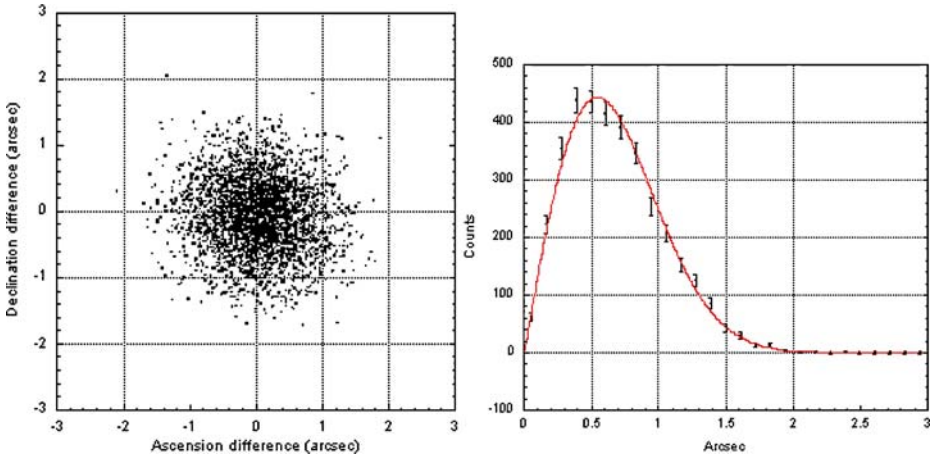

Fig. 12 Output of the numerical simulation on pointing precision using a 100 mm focal length optics. *left* The spatial spreading of the calculated pointing directions around the real target direction. *right* The radial distribution of the previous data: the curve fit gives a pointing precision value of 0.5430 ± 0.0046 arcsec

Table 4 Test data on the star identification software using simulated images: case with the additional focal lengths from 50 to 400 mm

Focal length (mm)	Num. of stars	Ident. rate	Calc. time (s)	Pointing precision (arcsec)
50	162–172	93.6%	$\bar{t} = 66.9 \pm 5.5$	0.6143 ± 0.0052
150	18–20	99.5%	$\bar{t} = 0.011 \pm 0.001$	0.5808 ± 0.0050
200	11–13	99.8%	$\bar{t} = 0.006 \pm 0.0002$	0.5718 ± 0.0050
300	6–8	99.7%	$\bar{t} = 0.004 \pm 0.0003$	0.5492 ± 0.0052
400	6	100%	$\bar{t} = 0.00470 \pm 0.00005$	0.4737 ± 0.0045

the latter shows that a sub-arcsec mean precision is feasible; the standard deviation value of the radial deviation is:

$$\sigma = 0.5430 \pm 0.0046 \text{ arcsec.} \tag{14}$$

Table 4 shows the data of the same simulation executed for different values of the focal length and therefore for different fields of view. The tracking algorithm was found to be successful for every focal length value.

The same table also shows the variation in the percentage of identified stars, and the calculation time. According to this table, we can conclude that the value of 100 mm chosen for the focal length, even for the less populated star fields, is the best value to have a sufficient number of visible stars and a high pointing precision, in a calculation time compatible with the required 1 Hz refresh cycle. The values of the pointing precision confirm the observations made in the previous paragraph: an increase of the focal length up to eight times the initial value of 50 mm, makes the pointing precision improve only by 23%.

8 Laboratory test

A laboratory test was carried out to verify the pointing precision suggested by the Monte Carlo simulation. Incidentally, this test also allowed additional evaluation of possible optical field distortion introduced by the optics. A test star field was simulated using point-like light sources made with 12 light emitting diodes (LED) fitted behind a screen to back-illuminate holes with a diameter of 0.3 mm. The screen was placed 10 m away from the camera. In this way the optics diffraction limit over the whole range of LED wavelengths from 430 to 880 nm resides within the pixel dimension, thus making these effectively acting as point-like sources. A focusing optimization was carried out to gain sufficient quantitative information for the design a motorized focusing system to be used in the final operating conditions and to evaluate the presence of chromatic aberration on the optics. The behaviour of the LEDs point spread function widths showed a "V" shape around the best focus position, with a diameter ranging from 0.6 to 1.5 pixels depending on light frequency. This position was spread over a mechanical excursion of the main focusing gear of 5°. Chromatic aberrations affect mainly blue and green wavelengths, but without consequences for the localization algorithm. In order to execute the star identification

algorithm, the LED angular distances were employed to generate a "LED catalogue" to replace the Hipparcos used in the previous numerical simulations. The pointing precision was calculated on a series of more than 80 images taken with a suitable exposure time to avoid pixel saturation. Furthermore, the screen was placed on a translation table fitted with a micrometer screw to simulate dynamical conditions and to avoid systematic errors due to illumination of the same CCD pixels. The screen was translated by steps of 10 μm (equivalent at an angular displacement of 0.2 arcsec at 10 m) between each acquisition.

The plots of Fig. 13(left) and (right) summarize the results of the laboratory test. These plots are the equivalent to those of Fig. 12(left) and (right); the fit on the radial distribution of the measured pointing direction shows a precision of:

$$\sigma = 0.86 \pm 0.05 \ \text{arcsec} . \tag{15}$$

This value gives the same order of magnitude (sub-arcsec) of (14). The slight discrepancy between these precision values can be explained by considering the dependence of this parameter with the number of captured stars in the two different tests. In fact, while up to 50 stars were available in the numerical simulation, only 12 "stars" were used in the laboratory test. Taking into account the plot of Fig. 11 (paragraph 6), and considering that the pointing error decreases with the inverse of the square root of the number of identified stars, the precision of the laboratory test is expected to be almost two times worse than the precision found in the simulated case. Indeed, the precision calculated in the laboratory test is approximately 1.6 times worse than the one of the simulation. These circumstances confirm that the scaling of the precision with the number of stars derived above is satisfactorily confirmed. As a final remark we observe that our laboratory tests did not show evidence of a significant optical field distortion due to our optics. Therefore optical field correction was not necessary.

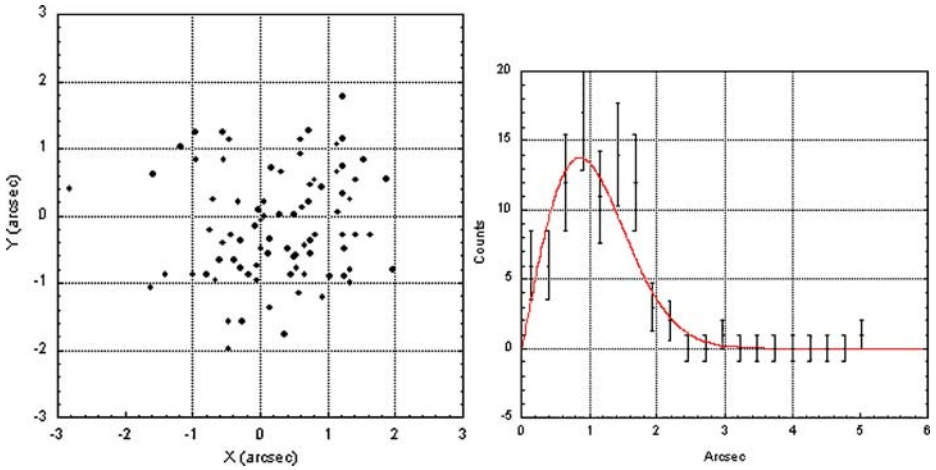

Fig. 13 Output of the laboratory test on pointing precision using a 100 mm focal length optics. *left* The spatial spreading of the calculated pointing directions around the real target direction. *right* The radial distribution of the previous data: the curve fit gives a pointing precision value of 0.86 ± 0.05 arcsec

9 Conclusions and acknowledgement

A detailed modelling of the performance of the HiPeG star sensor has been carried out using numerical and laboratory tools. Our modelling enables us to unfold the dependence of the pointing precision upon key system parameters including the number of stars in the field of view and the diameter of the star image. These laws are obtained by also taking into account the effect of spatial and intensity signal discretization on the centroid position of each star image. Our analysis shows that the set of custom developed algorithms is capable of providing the required arcsec level performance in the star identification process, as well as in the final pointing attitude reconstruction. The tracking test shows a high degree of robustness, with a calculation time compatible with the 1 Hz refresh rate. Finally, laboratory test carried out using multi-wavelength synthetic star fields, confirms these conclusions.

This work was carried out with financial support of the Italian Space Agency (ASI). We would like to thank A. Rossi and M. Voliani of IPCF-CNR for technical assistance. We acknowledge financial contribution from the MIUR-FISR project (Legge 449/97).

References

1. Di Cocco, G., Basili, A., Franceschini, T., Landini, G., Malaguti, G., Palladino, G., Silvestri, S., Gizzi, L.A., Barbini, A., Galimberti, M.: HiPeG: a high performance balloon gondola for fine angular resolution X-ray telescopes. In: Advances in Space Research, 35th COSPAR Proceedings, vol. 37, pp. 2103–2107 (2006)
2. Dietz, K.L., Ramsey, B.D., Alexander, C.D., Apple, J.A., Ghosh, K.K., Swift, W.R.: Daytime aspect camera for balloon altitudes. Opt. Eng. **41**, 2641–2651 (2002)
3. Rex, M., Chapin, E., Devlin, M.J., Gundersen, J., Klein, J., Pascale, E., Wiebe, D.: BLAST autonomous daytime star cameras published in Ground-based and Airborne Instrumentation for Astronomy. In: Proceedings of the SPIE, vol. 6269, pp. 62693H (2006). Opt. Eng. **41**, 2641–2651 (2006)
4. Fiore, F., Perola, G.C., Pareschi, G., Citterio, O., Anselmi, A., Comastri, A.: HEXIT-SAT: a mission concept for X-ray grazing incidence telescopes from 0.5 to 70 keV. SPIE Proc. **5488**, 933–943 (2004)
5. Galimberti, M., Gizzi, L.A., Barbini, A., Di Cocco, G., Basili, A., Franceschini, T., Landini, G., Silvestri, S.: Sviluppo del software di riconoscimento di un campo stellare. CNR internal report N. 1/122001 Prot. 817, I.F.A.M. – Pisa (2001)
6. Gunderson, K., Hubert Chen, C.M., Christensen, F., Craig, W., Decker, T., Hailey, C., Harrison, F.A., McLean, R., Wurtz, R., Ziock, K.: Ground performance of the high-energy focusing telescope (HEFT) attitude control system. SPIE Proc. **5165**, 158–168 (2004)
7. Harrison, F.A., Boggs, S.E., Di Bolotnikov, A., Christensen, F.E., Cook, W.R, Craig, W.W, Hailey, C.J., Jimenez-Garate, M., Mao, P.H., Schindler, S.E., Windt, D.L.: Development of the high-energy focusing telescope (HEFT) balloon experiment. SPIE Proc. **4012**, 693–699 (2000)
8. Padgett, C., Kretz-Delgado, K., Udomkesmalee, S.: Evaluation of star identification techniques. J. Guid. Control Dyn. **20**(2) (1997)
9. Ramsey, B.D., Alexander, C.D., Apple, J.A., Austin, R.A., Benson, C.M., Dietz, K.L., Elsner, R.F, Engelhaupt, D., Kolodziejczak, J.J., O'Dell, S.L., Speegle, C.O., Swartz, D.A., Weisskopf, M.C., Zirnstein, G.: HERO: high energy replicated optics for a hard x-ray balloon payload. SPIE Proc **4138**, 147–153 (2000)
10. Rossi, E., Di Cocco, G., Traci, A.: Progetto di un sensore stellare per la ricostruzione di assetto del telescopio GAMTEL. TESRE internal report N. 113 TESRE/IASF – Bologna (1986)